

ADVANCED MATERIALS

Supporting Information

for *Adv. Mater.*, DOI: 10.1002/adma.201907208

An Unconventional Transient Phase with Cycloidal Order
of Polarization in Energy-Storage Antiferroelectric PbZrO_3

Xian-Kui Wei, Chun-Lin Jia, Hong-Chu Du, Krystian
Roleder, Joachim Mayer, and Rafal E. Dunin-Borkowski*

Supporting Information for

**An Unconventional Transient Phase with Cycloidal Order
of Polarization in Energy-Storage Antiferroelectric PbZrO₃**

Xian-Kui Wei, Chun-Lin Jia, Hong-Chu Du, Krystian Roleder, Joachim Mayer, and Rafal E.
Dunin-Borkowski*

*Corresponding author. Email: x.wei@fz-juelich.de

Figure & Caption

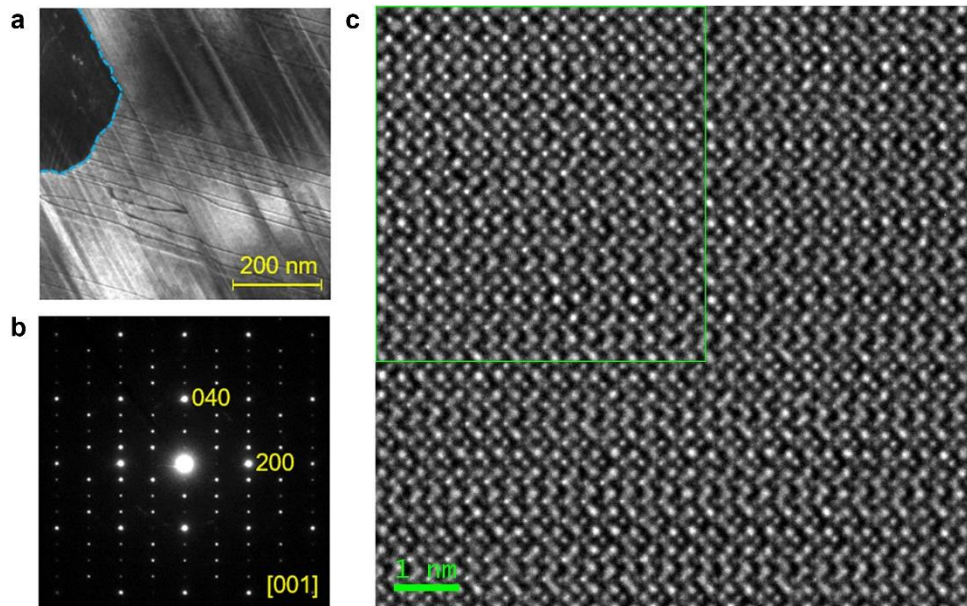


Figure S1. Atomic-resolution TEM image (#7) of PbZrO_3 recorded along the $[001]_O$ direction under the NCSI conditions. (a,b) Dark-field TEM image of PbZrO_3 crystal recorded using $(110)_O$ reflection and SAED pattern along the $[001]_O$ direction, respectively. The fine dark lines in bright region and blue dashed line denote the translation boundaries and a 90° domain boundary. (c) Positions of oxygen columns are mapped over the image to map the FD and AFD components. The rectangular region (green) highlights the region of interest used for quantitative TEM measurement, analysis and image simulation.

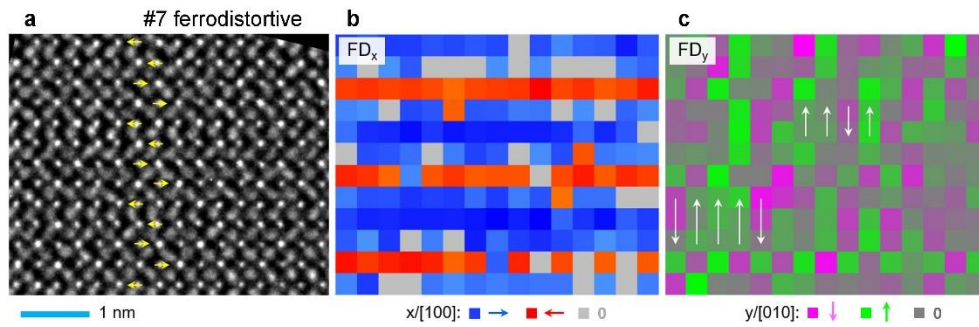


Figure S2. Complex FD texture. (a) Atom-resolved TEM image (#7) of the FE-FD phase in PbZrO_3 . The yellow arrows denote the antiparallel Pb displacements along the $[100]_O$ direction. (b,c) The FD_x and FD_y component map corresponding to the image area shown in (a). The white arrows denote development of local FE_y order together with the FE_x order in the FD phase.

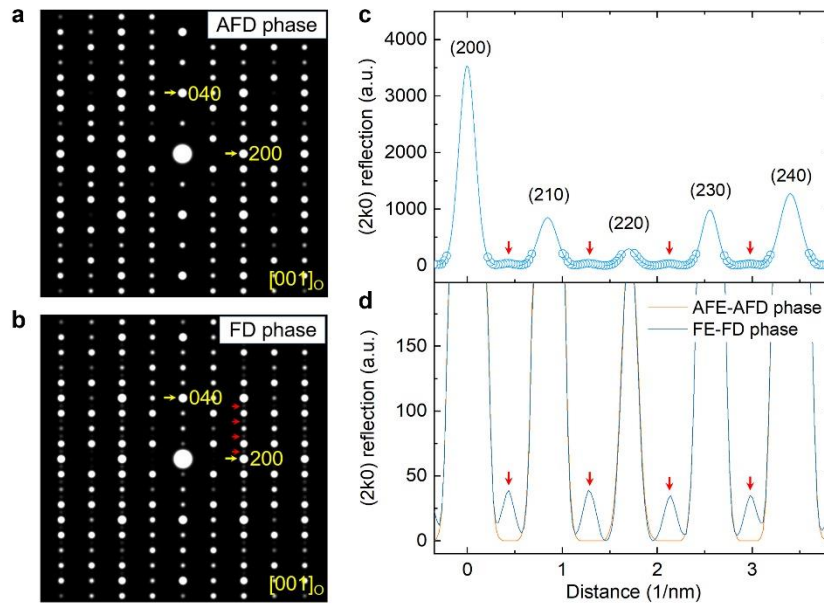


Figure S3. The FD order induced structure modulation. (a,b) Simulated SAED pattern of the AFE-AFD phase and the FE-FD phase along the $[001]_O$ direction with a specimen thickness of $t = 10$ nm, respectively. The reflections are indexed based on the AFE orthorhombic unit cell. (c,d) Intensity profile of the $(2k0)$ reflections and the magnified profile, respectively. The red arrows denote the superstructure reflections arising from the FD order, which is only $\sim 1\%$ of the (200) reflection in intensity.

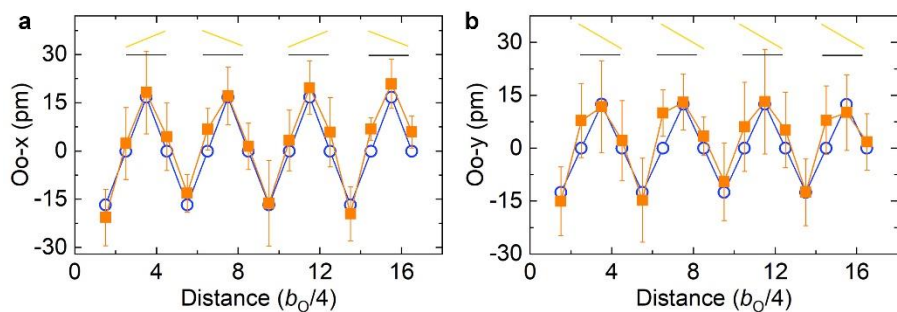


Figure S4. Atomic displacements. (a,b) The displacements of odd-column oxygen (Oo) atoms in the FE-FD phase (orange symbols) with that of the AFE-AFD phase (blue empty circles) for comparison. The orange line segments highlight the oxygen displacements as a result of the FD order with respect to the centrosymmetric positions (black line segments) in the AFD phase.

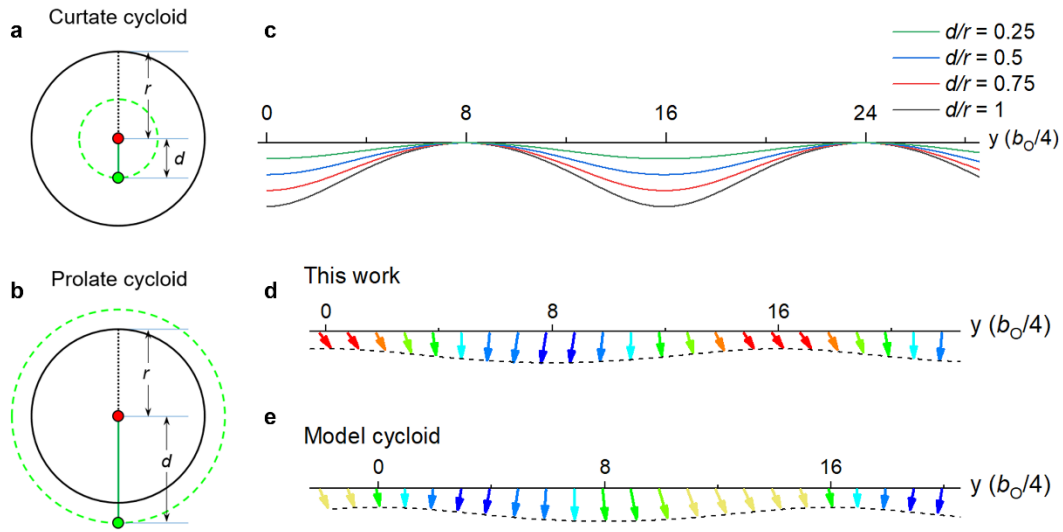


Figure S5. Cycloidal models and profiles. (a,b) Relationship of the fixed point (green symbol) with respect to radius (r) of the rolling circle for generation of curtate and prolate cycloid, respectively. (c) Curtate cycloidal profiles as a function of different d/r ratio. (d,e) The cycloidal polarization profile reported in this work and the standard model cycloid, which has parametric equations of $P_{SX} = r\phi - d\sin\phi$ and $P_{SY} = r - d\cos\phi$ (ϕ is the phase angle of the fixed point). Compared with the standard model, we noticed that a constant phase shift ($\phi_0 \approx \pi/2$) should be introduced to the P_{OY} equation to describe our cycloidal profile, i.e., $P_{SY} = r - d\cos(\phi - \phi_0) \approx r - d\sin(\phi)$, where the ratio is $d/r = 0.32$.

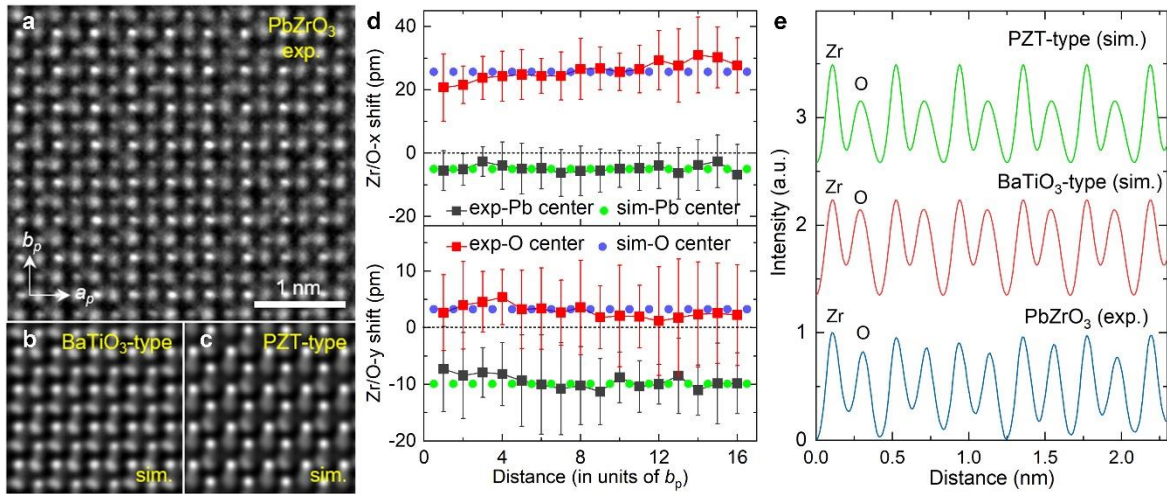


Figure S6. Experimental measurements and comparison. (a) Atom-resolved TEM image (#9) of PbZrO_3 shown in Fig. 4d. (b,c) Simulated image of PbZrO_3 in terms of rhombohedral- BaTiO_3 -type and PZT-type atomic displacements, respectively. (d) Measurement of Zr/O-column displacements with respect to centers of the nearest-neighboring Pb columns and the oxygen octahedral from the experimental and simulated image of (b). (e) Comparison of normalized intensity profiles of O-Zr/O-O atomic chains along the horizontal direction between the experimental and simulated images. It is noteworthy that the PZT-type monoclinic structure shown in (c) cannot fulfill the experimentally measured atomic displacements. Furthermore, a dramatic intensity reduction of oxygen can clearly be identified by comparing with the experimental and the rhombohedral- BaTiO_3 -type simulated profiles shown in (e).

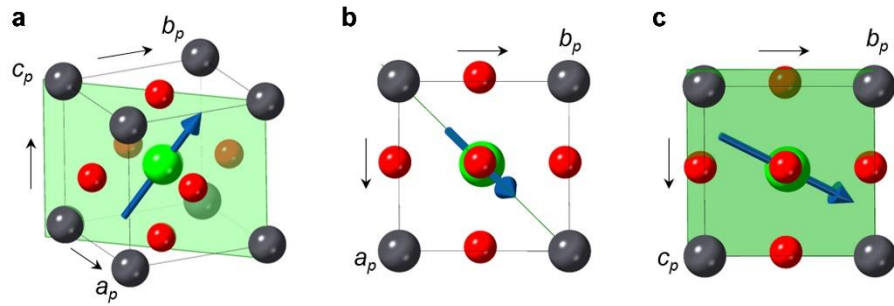


Figure S7. Identification of the PbZrO₃ FE monoclinic phase. (a) Stereo view of the monoclinic (M_A) phase with P_S (blue arrow) lying in between $[0\bar{1}0]_p$ and $[1\bar{1}\bar{1}]_p$ direction within the $(101)_p$ crystal plane. (b,c) Projection view of the monoclinic phase along $[010]_p$ and $[001]_p$ / $[001]_o$ direction, respectively. Thus, the results shown in Figure 4d suggest a FE monoclinic phase of the PbZrO₃ with lattice parameters of $a_p \approx b_p \approx c_p$.

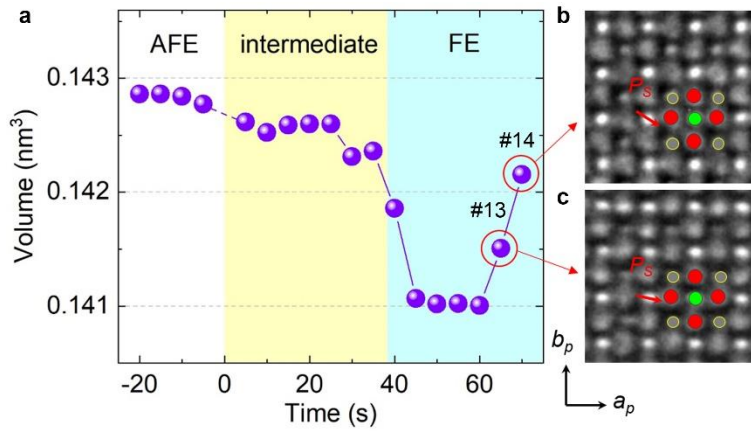


Figure S8. The FE_M - FE_R phase structure evolution after $t > 60$ s in $PbZrO_3$. (a) The volume change as a function of irradiation time. (b,c) Atomic resolution TEM images (numbered as #13 and #14) recorded along the $[001]_p$ direction in the time-resolution series, respectively. The displacement behaviors of oxygen columns (red circles) with respect to positions of Pb columns (grey circles) indicate a FE_M - FE_R phase transition associated with the volume expansion.

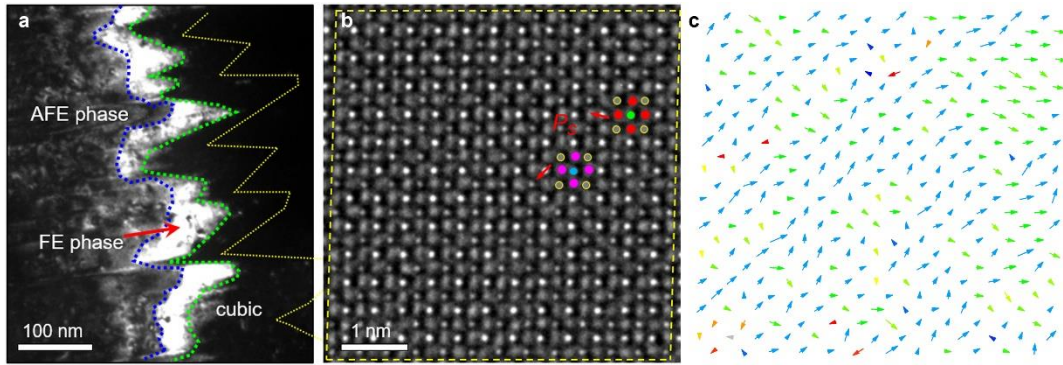


Figure S9. Sample thickness induced phase transition^[50,51] and structural constituent of the virgin FE state. (a) Distribution of the AFE and FE phases in the FIB-prepared lamella specimen. The thickness is decreasing from the AFE phase (left) towards the cubic (right) phase. (b,c) Atomic-resolution TEM image of the FE phase and corresponding mapping of oxygen displacements relative to the nearest-neighbor Pb-Pb columns, respectively. Coexistence of the FER phase (blue arrows in panel c) with the FEM phase (green arrows in panel c) at nanometer scale can be clearly seen. Our measurement shows that the lattice parameters are $a_R \approx b_R \approx 0.414$ nm in the FER-dominant region (left-side $\sim 2/3$ in panel c), and $a_M \approx 0.414$ nm and $b_R \approx 0.412$ nm in the FEM-dominant region (right-side $\sim 1/3$ in panel c), respectively.

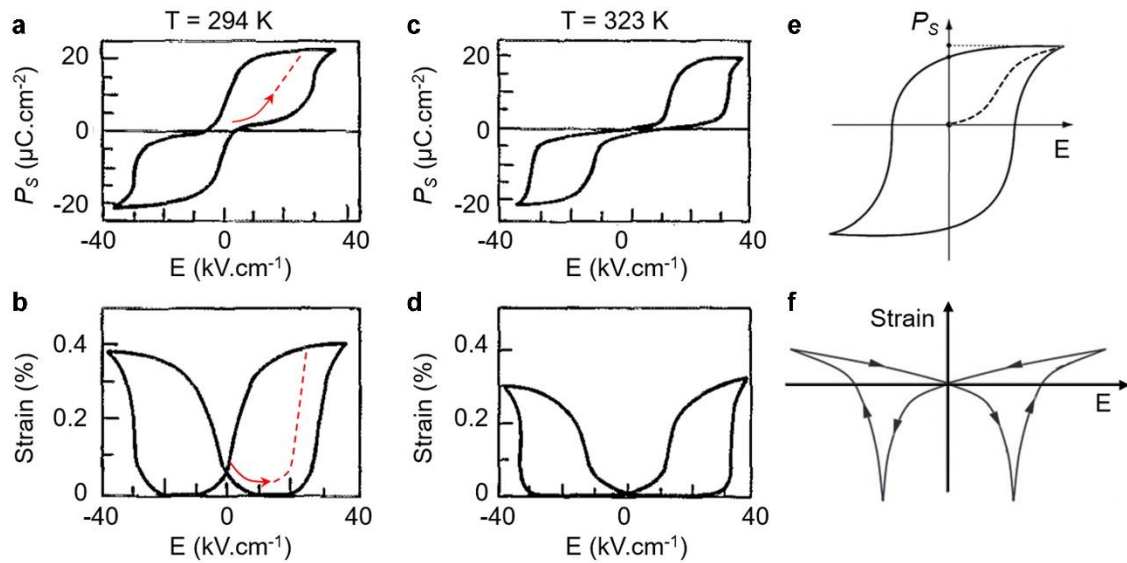


Figure S10. Comparison of electric field driven loops in AFEs and FEs. (a-d) The P-E and strain-E hysteresis loops of AFE $(\text{Pb}_{0.97}\text{La}_{0.02}\square_{0.01})(\text{Zr}_{0.66}\text{Sn}_{0.23}\text{Ti}_{0.11})\text{O}_3$ measured at 294 K (a,b) and 323 K (c,d), respectively, which are extracted from Ref. [14]. (e,f) The P-E and strain-E hysteresis loops of ordinary FE materials, e.g., the PZT referred from Ref. [8]. With respect to the observed polarization increment and volume change, the red arrows and dashed lines denote the phase-transition path of PbZrO_3 reported in this work.

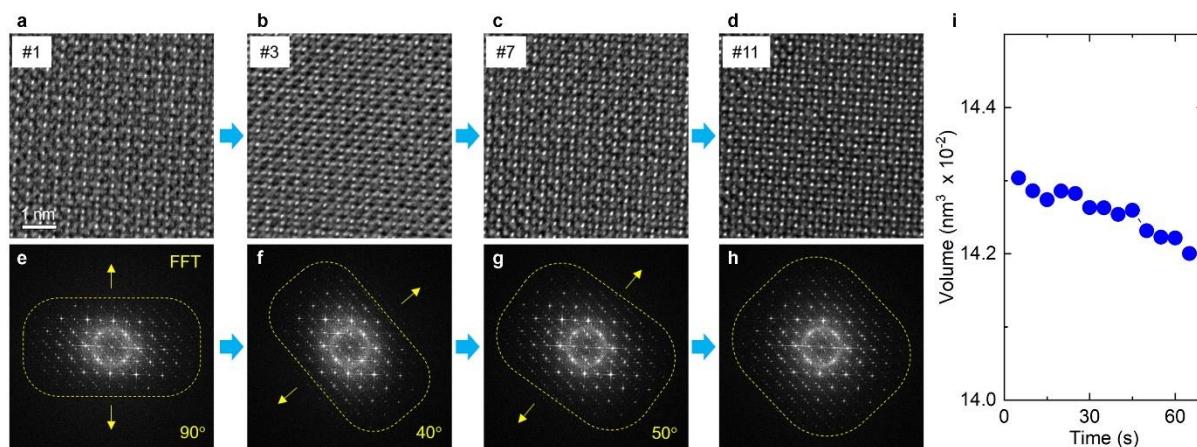


Figure 11. Illustration of strong charging effect during the high-resolution TEM experiments. (a-d) Sequential snapshots of atomic-resolution TEM images of AFE PbZrO₃ recorded along the [001]_O direction using the NCSI technique. The charging effect leads to clear elongation of Pb and Zr/O columns along certain directions. The oxygen columns even turn to streaks along certain directions. (e-h) Corresponding FFT images of the TEM images. The dashed rectangles denote the anisotropic intensity distribution in each FFT image and random orientation in the sequence as a result of charging. (i) The unit-cell volume (V) change of the AFE phase as a function of irradiation time.